Available online at www.sciencedirect.com
ScienceDirect
International Journal of Mass Spectrometry 263 (2007) 113–126
International Journal of Mass Spectrometry
www.elsevier.com/locate/ijms

Review

Secondary ion mass spectrometry of irradiated nuclear fuel and cladding: An overview

S. Portier*, S. Brémier, C.T. Walker

European Commission, Joint Research Centre, Institute for Transuranium Elements, P.O. Box 2340, D-76125 Karlsruhe, Germany

Received 29 June 2006; received in revised form 19 January 2007; accepted 22 January 2007
Available online 2 February 2007

Abstract

The principles and operating modes of secondary ion mass spectrometry (SIMS) are first described after which the different methods of quantification are summarised. Some current applications of SIMS in nuclear fuel and cladding research are then reviewed after briefly considering the modifications that are needed to allow a SIMS instrument to be used for the analysis of highly radioactive materials. Amongst the applications reported are the investigation of the behaviour of fission gas xenon and the volatile fission products tellurium, iodine and caesium in UO_2 nuclear fuel, measurement of the radial distribution of Pu isotopes in mixed oxide (MOX) fuel and of the radial distribution of Gd isotopes in $(U,Gd)O_2$ fuel, and determination of the distribution of Li and B in the external oxide layer on Zircaloy cladding. It is evident from the large amount of new information gained that SIMS is a powerful complementary technique to electron probe microanalysis (EPMA) in these fields of study.

Keywords: Secondary ion mass spectrometry; Shielded SIMS; Isobaric interference; Irradiated nuclear fuel; Zircaloy cladding

Contents

* Corresponding author. Tel.: +49 7247 951 124; fax: +49 7247 951 590.
E-mail address: Stephane.Portier@cec.eu.int (S. Portier).

1387-3806/$ – see front matter © 2007 Elsevier B.V. All rights reserved.
doi:10.1016/j.ijms.2007.01.016

1. Introduction

For the nuclear industry, the use of secondary ion mass spectrometry (SIMS) presents advantages of major importance for the analysis of irradiated nuclear materials: fast element imaging, high sensitivity for trace element (fission product) detection, accurate isotopic measurements and excellent depth resolution. Double-focusing sector field instruments are able to reach a mass resolution of up to 25,000 under favourable conditions. This ensures clear, accurate analyses by removing most isobaric interferences between the atomic ions of the analyte and, e.g., atomic and molecular ions at the same nominal mass. Depth resolution in the nanometre range and lateral resolution better than 0.2 μm in the microprobe mode permit the measurement of the radial distribution of fission products and actinide isotopes in high burn-up fuels. Additionally, a low detection limit of the order of 1 ppb makes the detection of minor isotopes possible.

Microbeam analysis of irradiated nuclear materials is carried out in many areas of nuclear technology, e.g., behaviour of fission products and decay products under normal and off-normal irradiation conditions (a reactor power transient), partitioning and transmutation, aqueous leaching of spent fuel and Zircaloy cladding corrosion. Today, in these different fields, electron probe microanalysis (EPMA) is the analytical technique commonly used [1]. EPMA, however, can no longer provide all the analytical data demanded by modern fuel performance research programmes. For example, EPMA cannot detect the fission gas Kr in nuclear fuel, nor can it detect the fission gas present in bubbles in the fuel larger than about 0.1 μm [2,3]. Moreover, the detection limit for the fission products is relatively high, varying between 200 and 500 ppm depending on the activity of the fuel sample and the analytical conditions, i.e., primary beam current and acquisition time. In addition, the elements H and Li cannot be analysed by EPMA, whereas Be, B, C, N and O may be analysed in favourable circumstances, but the accurate determination of their concentrations is difficult. Thus, EPMA is not suitable for the investigation of B and Li pick-up by the oxide layer on the outer surface of Zircaloy fuel cladding, the measurement of hydrogen penetration in Zircaloy cladding, or the measurement of the radial oxygen distribution in oxide fuel.

In contrast, using secondary ion mass spectrometry, the fission gas Kr can be detected as can the fission gas contained in gas bubbles and pores in the fuel matrix. Moreover, the qualitative analysis of all the elements with $Z<9$ can routinely be carried out. For convenience, the main characteristics of SIMS and EPMA are compared in Table 1.

Table 1
Technical characteristics of SIMS and EPMA

Parameter	SIMS	EPMA
Depth resolution (μm)	0.003	0.1
Lateral resolution (μm)	0.1–0.2	0.5
Analysed volume (μm^3)	10^{-2}–10^3	1.0
Elements range	All	$Z>3$[a]
Limit of detection (ppm)	0.001	200
Quantification	Difficult	±3%
Destructive	Yes	No

[a] The analysis of the fission gas Kr is not possible.

In the first part of the paper, the principles and operating modes of SIMS are described after which the different methods of quantification are considered. Some current applications of SIMS in nuclear fuel and cladding research are then reviewed after considering the modifications that are needed to allow a SIMS instrument to be used for the analysis of highly radioactive materials.

2. Technical aspects of SIMS

2.1. General principles

In SIMS, a secondary ion beam formed when an energetic beam of primary ions bombards the surface of a sample is analysed. The sputtered matter is mainly composed of neutral particles, but only ions are detected and analysed by the mass spectrometer. This process provides a mass spectrum of a surface from which its isotopic composition can be determined. SIMS analysis can be classified as static or dynamic according to the primary ion beam dose. Static SIMS uses a low primary ion flux density, typically $<10^{-13}$ cm^{-2}. In this type of analysis, it is necessary to maximise the information collected per unit of surface sputtered, which is characteristic of the chemistry of the surface layer, because statistically no point on the surface is impacted more than once by the primary ion beam. The main drawback is the very small number of secondary ions emitted which necessitates the use of a mass analyser with a high sensitivity. Dynamic SIMS exploits the destructive capability of the primary beam to analyse the chemical composition of materials as a function of depth. A high sensitivity for the element of interest and rapid erosion rates are major requirements, hence a high primary ion flux density is necessary. Depth profiles are obtained by recording the secondary ion current as a function of time; the time scale being then converted into a depth scale by calibration.

As pointed out by Betti [4], despite its qualities, SIMS has many deficiencies compared with others surface analysis techniques like EPMA and photoelectron spectrometry. The most important of these are:

- matrix effects, i.e., the sputtering yield of the studied species is influenced by its chemical environment;
- dependence on the mass spectrometer parameters, i.e., energy band-pass and transmission;
- dependence of detector efficiency on the element analysed;
- the existence of isobaric interferences.

2.2. Types of mass analysers

SIMS instruments fall into three categories defined by the type of mass analyser employed. The quadrupole analyser was first used in static SIMS. The device uses a combination of direct current and a radio-frequency electric field to separate ions according to their mass to charge ratio. It is, however, a low

transmission device (1%). Moreover, mass detection is sequential since it is a scanning instrument; all other masses being discarded. The Paul Scherrer Institute (PSI) in Switzerland was the first to carry out SIMS analysis of irradiated nuclear fuel. Their first shielded instrument installed in the late seventies was an ATOMIKA a-DIDA quadrupole SIMS [5]. This instrument had some major deficiencies, particularly in terms of isotope mapping and lateral resolution and in 1995 it was replaced by an ATOMIKA S4000, which is also a quadrupole mass analyser. The instrument is able to carry out static and dynamic SIMS analyses and has produced results in the form of depth profiles, line scans and ion maps (see, e.g., refs. [6,7]). Traditionally, double-focusing instruments have been used for dynamic SIMS because of their high transmission (10–50%) and high mass resolution (up to 25,000 under favourable conditions). In double-focusing SIMS, an electric field is used to extract the sputtered ions which are then energy and mass filtered by an electrostatic analyser and a magnet before going to the mass spectrometer for isotopic analysis. Double-focusing instruments can operate as an ion microscope or ion microprobe. In the ion microscope mode, a defocused static beam of primary ions is used so that each point on the sample surface is a source of secondary ions. All the secondary ions are received simultaneously by the detector. To select an isotope with a given mass the secondary ion signal is mass filtered. This mode is used for ion mapping. In the microprobe mode, the primary ion beam is focused to a spot 1–10 μm in diameter and raster scanned over the sample surface to produce a crater. This mode is used for acquiring mass spectra and depth profiles. A shielded version of a CAMECA IMS 6f double-focusing SIMS for the analysis of irradiated material has been in operation at the LECA laboratory of the CEA, Cadarache, France, since 1999 [8,9] and at the Institute for Transuranium Elements, since 2003 [10]. Relatively recently, time-of-flight (ToF) SIMS instruments have been introduced. Because of their very high transmission and the fact that they are equipped with a multi-detector that collects all the ions generated, they are used in the static mode. Up to now, the use of ToF SIMS has focused on the analysis of organic materials. This is because ToF SIMS employs a pulsed primary ion beam and offers a high negative ion yield and a mass resolution in the region of 5000–10,000 over a mass range of the order of 10,000 amu. The performances of the three types of mass analyser are compared in Table 2.

Table 2
The performance of different types of mass analysers

Parameter	Mass analyser		
	Quadrupole	Double-focusing	Time-of-flight
Ion detection mode	Sequential	Sequential	Parallel
Mass resolution	<400	300–2500	5000–10,000
Mass range[a] (amu)	<1000	460[b]	Unlimited[c]
Transmission (%)	<1	<50	80 max.[d]
Relative sensitivity[e]	1	10–30	<0.1

[a] The limit of m/z over which a mass spectrometer can detect ions.
[b] At 5 kV; max. 2000 amu (optional).
[c] In practice: 500 amu bulk; 10,000 amu monolayer.
[d] <40% for atomic ions; <80% for molecular ions.
[e] Sensitivity relative to that of the quadrupole analyser.

2.3. Modes of operation

The primary beam may consist of oxygen ions ($^{16}O_2^+$ or $^{18}O_2^+$, $^{16}O^-$ or $^{18}O^-$), caesium ions ($^{133}Cs^+$) argon ions ($^{40}Ar^+$) or gallium ions ($^{70}Ga^+$). The ions are focused on the sample by a series of electrostatic lenses and diaphragms. The ion beam properties (e.g., beam size, beam intensity, sample area excited) depend on the analysis mode, the studied species and the matrix. The secondary ion beam, consisting of ions sputtered from the surface of the sample, is analysed by an energy filter and a mass spectrometer.

At least five modes of operation can be distinguished on the basis of the instrument set up and the data treatment; namely, spectrum acquisition, depth profiling, line scanning, element mapping and isotope ratio measurement. In depth profiling the sample surface is sputtered in depth and a concentration profile of the analysed isotopes is obtained with a resolution of several nanometres, but the depth analysed is limited to a few micrometers. Line scanning gives similar information to depth profiling, but the distance traversed can be much greater (i.e., millimetres). In this mode, the spatial resolution is defined by the performance characteristics of the sample stage. Element mapping is used to reveal the distribution of a specific element or isotope in a given area of the sample.

The analytical conditions employed by different workers are listed in Table 3 according to the mode of operation employed. The analytical conditions used depend on the objective of the analysis, the performance of the instrument and the tuning achieved. Attention is drawn to the fact that most of the analyses have been carried out using an oxygen or caesium ion source. Hocking et al. [11], however, used an argon ion source for the analysis of $^{85}Rb^+$, $^{133}Cs^+$ and $^{84}Kr^+$, presumably, to avoid the contamination of the sample with Cs. Moreover, Gebhardt et al. [6,12] used a gallium primary ion source for ion mapping of $^7Li^+$, $^{11}B^+$ and $^{52}Cr^+$ in the external oxide layer on Zircaloy. As seen from Table 3, a beam diameter of less than 100 nm can be achieved with a gallium ion source and consequently elements maps produced with this type of source have a high spatial resolution.

2.4. Mass resolution

The mass spectrometric separation of isobaric interferences of atomic ions of the analyte with, e.g., atomic or molecular ions at the same nominal mass is possible if the mass resolution is sufficient. The required mass resolution, $(MR)_{ij}$, is given by the following equation:

$$(MR)_{ij} = \frac{m_i}{|m_i - m_j|} \quad (1)$$

where m_i is the mass of the analyte ions and m_j is the mass of the interfering ions.

The mass resolution of the secondary ion optical system of a SIMS instrument, MR, under the specific analytical conditions

Table 3
Conditions employed for the analysis of fission products, actinide elements, Zircaloy constituents and light water coolant additives (Li and B) classified according to the mode of analysis

Ion	Matrix	Mass analyser	Primary beam	Beam current (nA)	Beam size (μm)	Raster size (μm)	Ref.
Depth profiling							
$^{129}Xe^+$	UO_2	Double-focusing	$(^{16}O)_2^+$	1000	30	200	[20]
$^{132}Xe^+$	UO_2	Double-focusing	$(^{16}O)_2^+$	20	30	None	[21]
$^{127}I^-$	UO_2	Double-focusing	$^{133}Cs^+$	30–100	200	250	[27]
$^{85}Rb^+$	UO_2	Double-focusing	$^{40}Ar^+$	300	–	2000	[11]
$^{133}Cs^+$	UO_2	Double-focusing	$^{40}Ar^+$	300	–	2000	[11]
$^{84}Kr^+$	UO_2	Double-focusing	$^{40}Ar^+$	300	–	2000	[11]
$^{1}H^-$	Zr + Nb	Double-focusing	$^{133}Cs^+$	800–2000	60	250	[49]
$^{2}D^-$	Zr + Nb	Double-focusing	$^{133}Cs^+$	800–2000	60	250	[49]
$^{7}Li^-$	Zr + Nb	Double-focusing	$^{133}Cs^+$	800–2000	60	250	[49]
$^{19}F^-$	Zr + Nb	Double-focusing	$^{133}Cs^+$	800–2000	60	250	[49]
$^{90}Zr^-$	Zr + Nb	Double-focusing	$^{133}Cs^+$	800–2000	60	250	[49]
$^{106}ZrO^-$	Zr + Nb	Double-focusing	$^{133}Cs^+$	800–2000	60	250	[49]
$^{7}Li^+$	Zircaloy	Quadrupole	$(^{18}O)_2^+$	20–100	2–8	30	[7,35]
$^{11}B^+$	Zircaloy	Quadrupole	$(^{18}O)_2^+$	20–100	2–8	30	[7,35]
$^{106}ZrO^+$	Zircaloy	Quadrupole	$(^{18}O)_2^+$	20–100	2–8	30	[7,35]
$^{16}O^-$	UC	Double-focusing	$^{133}Cs^+$	50	–	250	[50]
Ion mapping							
$^{7}Li^+$	Zircaloy	Quadrupole	$^{70}Ga^+$	0.1	0.05	20	[6]
$^{11}B^+$	Zircaloy	Quadrupole	$^{70}Ga^+$	0.1	0.05	20	[6]
$^{106}ZrO^+$	Zircaloy	Quadrupole	$^{70}Ga^+$	0.1	0.05	20	[6]
$^{52}Cr^+$	Zircaloy	Quadrupole	$^{70}Ga^+$	0.1	<0.1	10	[12]
$^{56}Fe^+$	Zircaloy	Quadrupole	$^{70}Ga^+$	0.1	<0.1	10	[12]
$^{7}Li^-$	Zircaloy	Double-focusing	$(^{16}O)_2^+$	–	–	–	[8]
$^{52}Cr^+$	Zircaloy	Double-focusing	$(^{16}O)_2^+$	–	–	–	[8]
$^{56}Fe^+$	Zircaloy	Double-focusing	$(^{16}O)_2^+$	–	–	–	[8]
$^{90}Zr^+$	Zircaloy	Double-focusing	$(^{16}O)_2^+$	–	–	–	[8]
$^{129}I^-$	UO_2	Double-focusing	$(^{16}O)_2^+$	–	–	–	[24]
$^{130}Te^-$	UO_2	Double-focusing	$(^{16}O)_2^+$	–	–	–	[24]
$^{137}Cs^+$	UO_2	Double-focusing	$(^{16}O)_2^+$	–	–	–	[24]
$^{238}UO^+$	UO_2	Double-focusing	$(^{16}O)_2^+$	–	–	–	[24]
$^{92}Zr^+$	UO_2	Double-focusing	$(^{16}O)_2^+$	–	–	–	[23]
$^{139}LaO^+$	UO_2	Double-focusing	$(^{16}O)_2^+$	–	–	–	[23]
$^{7}Li^+$	Boron carbide	Quadrupole	$^{133}Cs^+$	120	–	50	[35]
$^{10}B^+$	Boron carbide	Quadrupole	$^{133}Cs^+$	120	–	50	[35]
$^{11}B^+$	Boron carbide	Quadrupole	$^{133}Cs^+$	120	–	50	[35]
Line scanning							
^{242}Pu[a]	UO_2	Quadrupole	$(^{16}O)_2^+$	200	50	–	[30]
^{241}Pu[a]	UO_2	Quadrupole	$(^{16}O)_2^+$	200	50	–	[30]
^{240}Pu[a]	UO_2	Quadrupole	$(^{16}O)_2^+$	200	50	–	[30]
^{239}Pu[a]	UO_2	Quadrupole	$(^{16}O)_2^+$	200	50	–	[30]
^{148}Nd[a]	UO_2	Quadrupole	$(^{16}O)_2^+$	200	50	–	[30]
^{143}Nd[a]	UO_2	Quadrupole	$(^{16}O)_2^+$	200	50	–	[30]
^{141}Pr[a]	UO_2	Quadrupole	$(^{16}O)_2^+$	200	50	–	[30]
^{140}Ce[a]	UO_2	Quadrupole	$(^{16}O)_2^+$	200	50	–	[30]
^{139}La[a]	UO_2	Quadrupole	$(^{16}O)_2^+$	200	50	–	[30]
^{138}Ba[a]	UO_2	Quadrupole	$(^{16}O)_2^+$	200	50	–	[30]
^{137}Cs[a]	UO_2	Quadrupole	$(^{16}O)_2^+$	200	50	–	[30]
^{133}Cs[a]	UO_2	Quadrupole	$(^{16}O)_2^+$	200	50	–	[30]
^{88}Sr[a]	UO_2	Quadrupole	$(^{16}O)_2^+$	200	50	–	[30]
$^{85}Rb^+$	UO_2	Quadrupole	$(^{16}O)_2^+$	200	50	–	[30]
$^{154}Gd^+$	UO_2	Quadrupole	$(^{16}O)_2^+$	50	10	–	[28]
$^{155}Gd^+$	UO_2	Quadrupole	$(^{16}O)_2^+$	50	10	–	[28]
$^{156}Gd^+$	UO_2	Quadrupole	$(^{16}O)_2^+$	50	10	–	[28]
$^{157}Gd^+$	UO_2	Quadrupole	$(^{16}O)_2^+$	50	10	–	[28]
$^{158}Gd^+$	UO_2	Quadrupole	$(^{16}O)_2^+$	50	10	–	[28]
$^{129}I^-$	UO_2	Double-focusing	$(^{16}O)_2^+$	–	–	–	[24]
$^{130}Te^-$	UO_2	Double-focusing	$(^{16}O)_2^+$	–	–	–	[24]
$^{1}H^-$	Zircaloy	Quadrupole	$(^{18}O)_2^+$	–	0.3	–	[51]
$^{16}O^-$	Zircaloy	Quadrupole	$(^{18}O)_2^+$	–	0.3	–	[51]

Table 3 (*Continued*)

Ion	Matrix	Mass analyser	Primary beam	Beam current (nA)	Beam size (μm)	Raster size (μm)	Ref.
Isotope ratio							
$^{234}U/^{238}U$	UO_2	Double-focusing	$(^{16}O)_2^+$	100–200	0.5–2	–	[47]
$^{235}U/^{238}U$	UO_2	Double-focusing	$(^{16}O)_2^+$	100–200	0.5–2	–	[47]
$^{231}Pa/^{235}U$	UO_2	Double-focusing	$(^{16}O)_2^+$	100–200	0.5–2	–	[47]
$^{234}U/^{230}Th$	UO_2	Double-focusing	$(^{16}O)_2^+$	100–200	0.5–2	–	[47]
$^{240}Pu/^{239}Pu$	PuO_2	Double-focusing	$(^{16}O)_2^+$	1–2	0.5–2	250	[47]
$^{238}Pu/^{234}U$	PuO_2	Double-focusing	$(^{16}O)_2^+$	1–2	~5	250	[44]
$^{239}Pu/^{235}U$	PuO_2	Double-focusing	$(^{16}O)_2^+$	1–2	~5	250	[44]
$^{240}Pu/^{236}U$	PuO_2	Double-focusing	$(^{16}O)_2^+$	1–2	~5	250	[44]
$^{18}O/^{16}O$	UO_2	Double-focusing	$^{133}Cs^+$	5–10	–	–	[48]

[a] The species used is not reported.

employed is given by:

$$\mathrm{MR} = \frac{m_i}{\Delta m_i} \tag{2}$$

where Δm_i is the width of the peak of analyte mass at 10% of the maximum intensity value. Burdo and Morrison [13] have compiled a list of the mass resolution necessary to analyse several hundred species, including simple ions, complex ions and clusters.

Table 4 lists some major isobaric interferences for the fission products and actinide isotopes encountered in irradiated nuclear fuel and the theoretical mass resolution needed for separation obtained from Eq. (1). It can be seen that for separation of all the interferences listed, a mass resolution that is much higher than that provided by a quadrupole mass analyser is required (see Table 2). Indeed, in a number of cases, the theoretical mass resolution needed is substantially higher than that of a double-focusing analyser, e.g., $^{154}Sm^+/^{154}Gd^+$, 1.5×10^5; $^{241}Pu^+/^{241}Am^+$, 1.1×10^7.

2.5. Quantification methods

The main challenge for laboratories using SIMS in the post irradiation examination of nuclear fuel is to convert the intensity of the mass peaks characteristic of the fission products and minor actinides (Np, Am and Cm) to concentration. Quantification methods are applied mainly in dynamic SIMS. In principle, the mass intensities measured during depth profiling can be quantified using one of three methods: comparison with a standard, use of relative sensitivity factors or by the use of the relative useful yield. Whatever the method employed, it should be kept in mind that quantification by SIMS is fundamentally empirical and that there is not yet a first principle formulation to predict sputtering yields of elements in a matrix of arbitrary composition.

2.5.1. Comparison with a standard

The main drawback of this method is the difficulty of preparing appropriate standards, especially for the analysis of fission products in irradiated nuclear fuel. The problem arises because the host matrix of the standard and sample should be similar, both in terms of chemical composition and microstructure. These requirements are difficult to meet for samples of irradiated nuclear fuel, which contain a large number of elements and exhibit substantial variations in microstructure [14]. Moreover, measurements on the standard have to be performed for each set of analytical conditions employed. Nevertheless, if a suitable standard is available accurate quantification can be performed.

2.5.2. Application of relative sensitivity factors

This method permits the concentration of an isotope to be calculated without systematic measurements on standards. The relative sensitivity factor, RSF, is defined [15] as:

$$\mathrm{RSF} = \frac{I_\mathrm{m}}{I_i}\rho_i \tag{3}$$

where I_m is the matrix isotope secondary ion intensity in c/s, I_i the impurity isotope secondary ion intensity in c/s and ρ_i is the impurity atom density in atoms cm^{-3}. RSFs can be determined experimentally [16,17] using the expression:

$$\mathrm{RSF} = \frac{F_i C I_\mathrm{m} t}{d\sum I_i - d I_\mathrm{b} C} \tag{4}$$

where F_i is the ion-implanted fluence of element i in atoms cm^{-2}, C the number of measurement cycles, d the crater depth, $\sum I_i$ the sum of the impurity isotope secondary ion counts over the depth profile, I_b the background ion intensity of I_i in counts per measurement cycle and t is the analysis time for the studied species.

For a specific isotope, the RSF can be calculated by using an implanted standard with a known fluence. This RSF is then used to calculate concentration of the isotope in samples with a similar matrix.

2.5.3. Application of relative useful yield

Phinney [18] has developed a simple method to quantify trace isotopes measured by SIMS analysis which involves comparing the ion signal coming from a trace element with the signal from a major element of known concentration. The useful yield, τ_i, of species, i, can be defined as:

$$\tau_i = \frac{D_i}{S_i} \tag{5}$$

where D_i is the number of ions of species i detected and S_i is the number of atoms of species i sputtered. S_i can be determined experimentally by measuring the depth of the crater (formed with a constant primary current intensity) in a standard implanted

Table 4
Some fission product and actinide isotope isobaric interferences and the theoretical mass resolution required for separation

Ion	Mass	Interference	Mass	$m/\Delta m$
Fission products				
$^{85}Kr^+$	84.9125	$^{85}Rb^+$	84.91202	176,901
$^{90}Sr^+$	89.9077	$^{90}Zr^+$	89.9043	26,443
		$^{89}YH^+$	89.9135	15,501
$^{96}Zr^+$	95.9093	$^{96}Ru^+$	95.9087	159,849
		$^{95}MoH^+$	95.9123	31,970
		$^{96}Mo^+$	95.905	22,304
		$^{94}ZrH_2^+$	95.9220	7,552
$^{97}Mo^+$	96.9062	$^{96}MoH^+$	96.9128	14,683
		^{96}ZrH	96.9171	8,890
$^{98}Mo^+$	97.906	$^{97}MoH^+$	97.9140	12,238
		$^{96}ZrH_2^+$	97.9249	5,180
$^{100}Mo^+$	99.9065	$^{100}Ru^+$	99.905	66,604
$^{104}Ru^+$	103.9042	$^{104}Pd^+$	103.9033	115,449
		$^{88}SrO^+$	103.901	32,470
$^{105}Pd^+$	104.9048	$^{89}YO^+$	104.9006	2,497
$^{124}Xe^+$	123.9061	$^{124}Sn^+$	123.9052	137,673
$^{126}Xe^+$	125.9045	$^{126}Sn^+$	125.9077	39,345
		$^{110}PdO^+$	125.8994	24,687
		$^{110}CdO^+$	125.8982	19,985
$^{127}I^-$	126.9047	$^{1}CdO^-$	126.8992	23,074
$^{128}Xe^+$	127.9035	$^{112}CdO^+$	127.898	23,255
$^{129}I^-$	128.905	$^{113}CdO^-$	128.8994	23,019
		$^{97}MoO_2^-$	128.896	14,323
$^{134}Cs^+$	133.9067	$^{134}Xe^+$	133.0954	103,005
		$^{134}Ba^+$	133.9042	53,563
		$^{102}RuO_2^+$	133.8935	10,144
$^{136}Xe^+$	135.9071	$^{136}Ba^+$	135.9044	48,538
$^{137}Cs^+$	136.9071	$^{137}Ba^+$	136.9056	91,271
$^{138}Ba^+$	137.9049	$^{137}BaH^+$	137.9134	16,224
$^{139}La^+$	138.906	$^{138}BaH^+$	138.9127	20,732
$^{140}Ce^+$	139.9053	$^{139}LaH^+$	139.9139	16,268
		$^{108}PdO_2^+$	139.8933	11,659
$^{141}Pr^+$	140.9075	$^{140}CeH^+$	140.9131	25,162
$^{142}Ce^+$	141.9093	$^{142}Nd^+$	141.9075	78,838
		$^{110}PdO_2^+$	141.8943	9,461
		$^{110}CdO_2^+$	141.8931	8,760
$^{143}Nd^+$	142.9096	$^{142}NdH^+$	142.9153	25,072
		$^{142}CeH^+$	142.9171	19,055
$^{144}Nd^+$	143.9098	$^{143}NdH^+$	143.9174	18,936
^{145}Nd	144.9121	$^{144}NdH^+$	144.9176	26,348
$^{146}Nd^+$	145.9127	$^{145}NdH^+$	145.9199	20,266
$^{147}Sm^+$	146.9145	$^{146}NdH^+$	146.9205	24,486
$^{148}Nd^+$	147.9165	$^{148}Sm^+$	147.9144	70,436
		$^{116}CdO_2^+$	147.8948	6,816
$^{150}Nd^+$	149.9208	$^{150}Sm^+$	149.9169	38,441
$^{154}Sm^+$	153.9219	$^{154}Gd^+$	153.9209	153,922
		$^{154}Eu^+$	153.923	139,929
		$^{138}BaO^+$	153.8998	6,965
$^{160}Gd^+$	159.9271	$^{160}Dy^+$	159.9239	49,977
		$^{144}NdO^+$	159.9048	7,172
		$^{128}TeO_2^+$	159.8535	2,173
Actinides				
$^{234}U^+$	234.0403	$^{233}UH^+$	234.0474	32,963
$^{235}U^+$	235.0428	$^{234}UH^+$	235.0481	44,348
		$^{233}UH_2^+$	235.0552	18,955
$^{236}U^+$	236.0456	$^{235}UH^+$	236.0506	47,209
		$^{234}UH_2^+$	236.0559	22,917
$^{237}Np^+$	237.0482	$^{236}UH^+$	237.0534	43,898
$^{238}U^+$	238.0486	$^{236}UH_2^+$	238.0612	18,893
		$^{238}Pu^+$	238.0496	240,000
		$^{237}NpH^+$	238.0561	31,740
$^{239}Pu^+$	239.0522	$^{238}UH^+$	239.0564	56,917
$^{240}Pu^+$	240.0538	$^{238}UH_2^+$	240.0642	23,082
		$^{239}PuH^+$	240.0600	38,720
$^{241}Pu^+$	241.0569	$^{241}Am^+$	241.0568	10,907,550
		$^{240}PuH^+$	241.0616	50,695
$^{242}Pu^+$	242.0587	$^{241}AmH^+$	242.0646	41,027
		$^{241}PuH^+$	242.0646	41,027
$^{243}Am^+$	243.0614	$^{242}PuH^+$	243.0665	47,659
		$^{241}AmH_2^+$	243.0724	22,096
		$^{241}PuH_2^+$	243.0724	22,096
$^{244}Cm^+$	244.0743	$^{243}AmH^+$	244.0692	37,548
		$^{242}PuH_2^+$	244.0743	21,040

with the species i. The main weakness of the useful yield is its dependence on the extrinsic properties of the SIMS instrument [18], such as aperture diameters and slit width. To remove this difficulty, Phinney proposed to use the relative useful yield (RUY). This is defined as:

$$[\mathrm{RUY}]_{ij} = \frac{\tau_j}{\tau_i} \tag{6}$$

where $[\mathrm{RUY}]_{ij}$ is the relative useful yield of species i with respect to species j and τ_i is the useful yield of species i and τ_j the useful yield of species j.

For a material with a known RUY, the unknown concentration of species i, C_i, can be obtained from:

$$C_i = \frac{D_i}{D_j} \times [\mathrm{RUY}]_{ij} \times C_j \tag{7}$$

where D_j is the number of ions detected of species j and C_j is the concentration of the major species j (atoms j/atoms matrix). In most cases, C_j can be obtained by EPMA.

There are two ways to measure the RUY by SIMS. By using a standard with a homogeneous distribution of the trace element species (bulk standard) or by using a standard implanted with the trace element species (implanted standard). For bulk-standards, ion signals from species i and species j are constant and the RUY is defined as:

$$[\mathrm{RUY}]_{ij} = \frac{\sum D_j}{\sum D_i} \frac{n_i}{n_j} \tag{8}$$

where n_i and n_j are the atom densities of species i and j, respectively. For implanted standards, the ion signal of j is constant,

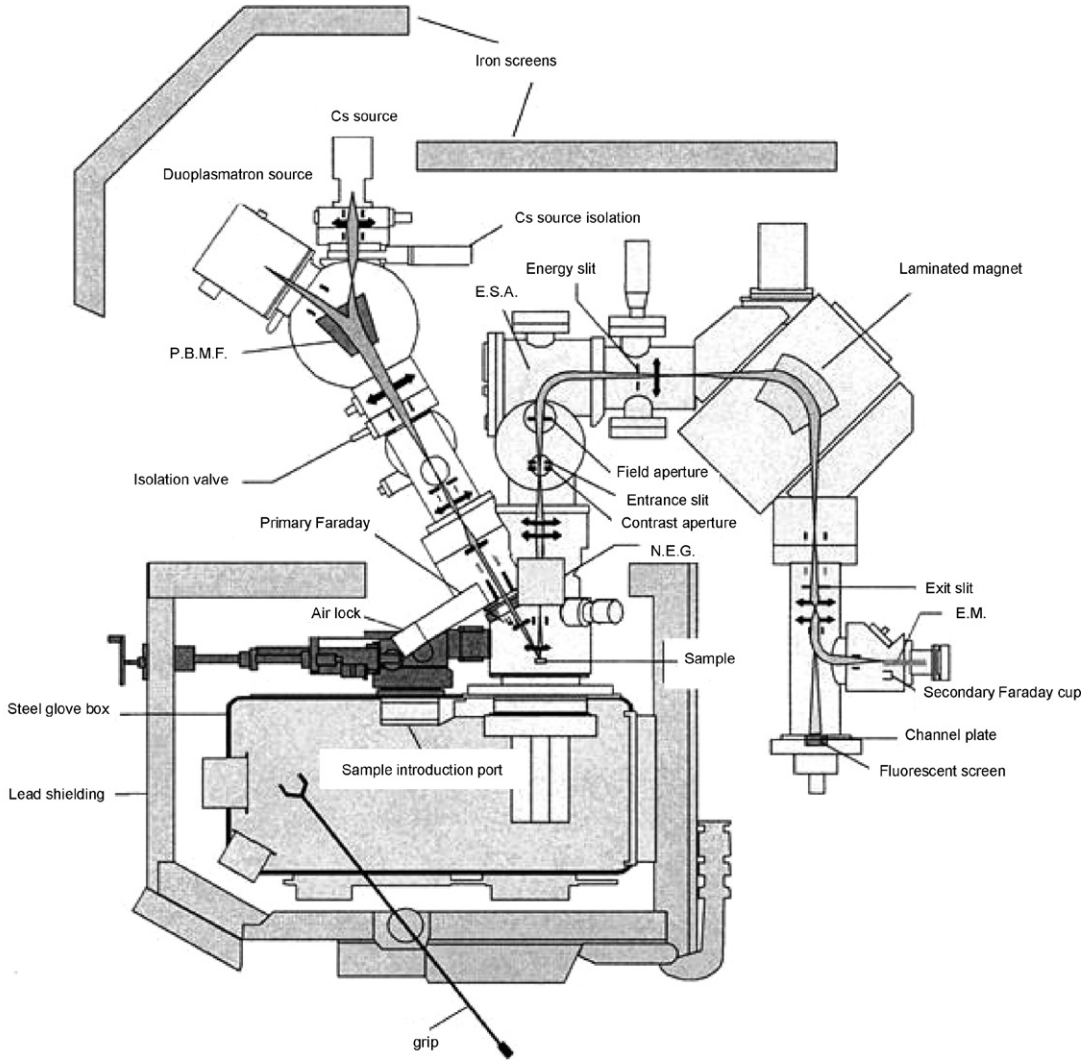

Fig. 1. General diagram of the shielded CAMECA IMS-6f SIMS showing the steel glove box housing the sample introduction port and the arrangement of the iron and lead shielding (courtesy of CAMECA, France).

whereas that of i varies. In this case, the sum of D_i has to be calculated by numerical integration over the implantation Gaussian. The RUY is then given by:

$$[\mathrm{RUY}]_{ij} = \frac{\sum_{d_0}^{d_1} D_j}{\int_{d_0}^{d_1} D_i} \frac{F_i}{n_j(d_1 - d_0)}. \quad (9)$$

3. The shielded SIMS

A SIMS instrument dedicated to the analysis of irradiated nuclear materials needs several modifications to protect laboratory personnel and electronic components from the gamma and beta radiation, emitted by the sample, and from radioactive contamination. The specimen chamber and introduction airlock has to be enclosed in a glove-box to restrict the spread of alpha and beta contamination during sample transfer and loading. Moreover, since SIMS is a destructive technique, over time the immersion lens of the instrument accumulates alpha and beta contaminated. General maintenance of the instrument and removal for cleaning or disposal of contaminated parts is carried out via the glove-box. Heavy metal shielding has to be installed around the instrument and the slits and diaphragms of both the primary column and secondary optics axis need to be motorised to avoid manual intervention while a radioactive sample is in the instrument. The modifications made to the first ATOMIKA a-DIDA instrument installed at PSI and the shielded Cameca IMS 6f instrument installed at the CEA Cadarache and ITU Karlsruhe for SIMS analysis of irradiated nuclear fuel are described in refs. [5,8,10]. Fig. 1 shows a diagram of a shielded CAMECA IMS 6F instrument similar to the one installed at the Institute for Transuranium Elements. This installation permits the analysis of nuclear fuel samples with a gamma activity up to 75 GBq (2 Ci).

4. Current applications

4.1. Analysis of the fission gas xenon

Ray et al. [19] report that the ionisation of rare gases is too low to be measured when using a caesium primary ion beam,

but that $(CsR)^+$ complex ion creation, where R is a rare gas ion, was sufficient to obtain good results. They also demonstrate that $(CsR)^+$ complexes are formed by surface ionisation processes, while R^+ ions are formed by inelastic collisions involving rare gas atoms released from the sample with thermal velocities. R^+ ions can be measured using an oxygen beam and an oxygen leak to increase their production.

The inert gas xenon is the most abundant fission product produced during irradiation. Xenon retained in bubbles in the fuel has an important impact on the fuel behaviour in terms of heat conductivity and in-pile swelling. More precise data on the partitioning of retained xenon between gas bubbles, grain boundaries and the fuel matrix is one of the main objectives of the application of SIMS to irradiated nuclear fuel.

Desgranges and Pasquet [20] have shown that xenon in a UO_2 matrix can be detected by SIMS as Xe^+ by using a $O_2{}^+$ primary ion beam, an oxygen leak and a positive offset voltage to increase the secondary ion current. These analyses were performed on a UO_2 single crystal implanted with xenon (5×10^{15} at/cm^2, 540 keV) exhibiting a maximum concentration at a calculated depth of 100 nm and polycrystalline UO_2 implanted with xenon (5×10^{15} at/cm^2, 800 keV) with a maximum concentration at 126 nm. In the same article, Desgranges and Pasquet also show that xenon sputtered from UO_2 is not ionised at the sample surface as is commonly the case in SIMS, but in the vacuum above the sample surface, as is the case for the rare gases argon and krypton in semiconductors [19]. The ionisation mechanism is independent of the origins of the xenon (i.e., independent of whether it results from the UO_2 matrix or from gas bubbles) and exhibits an $aJ^2 + bJ$ dependence, where J is the current density and a and b are coefficients depending on physical constants, sample characteristics (e.g., xenon concentration) and oxygen flooding. The authors state that the coefficients a and b vary linearly with xenon concentration, and conclude that this allows quantification, although no detailed explanation is given.

Furthermore, Desgranges and co-workers [21,22] have shown that it is possible to distinguish between xenon coming from the matrix and from gas bubbles during depth profiling. Fig. 2 shows the variation of the intensity of the $^{132}Xe^+$ mass peak as a function of sputtering time (erosion rate) for a section of irradiated UO_2 fuel from a PWR fuel rod with a burn-up of about 60 MWd/kgHM. It can be seen that the profile obtained from a region in the fuel where gas bubbles were visible in the scanning electron microscope (Fig. 2a) exhibited numerous intensity peaks that denote the location of bubbles, whereas the profile obtained from a region where gas bubbles were absent (Fig. 2b) is flat and exhibits minor variations in intensity only. The same group have also devised a method to quantify the xenon ion intensities emitted from the gas bubbles in irradiated UO_2 [21]. This involves calibrating the xenon ion signal using the concentration of gas in the UO_2 matrix measured by EPMA.

As can be seen from Fig. 3 a dependence of the sputtering yield on the crystallographic orientation of the grain was observed by Desgranges and Pasquet [23]. This has important implications for quantification procedures involving a standard. Accurate quantification cannot be guaranteed unless both the sample and standard are single crystals with the same orienta-

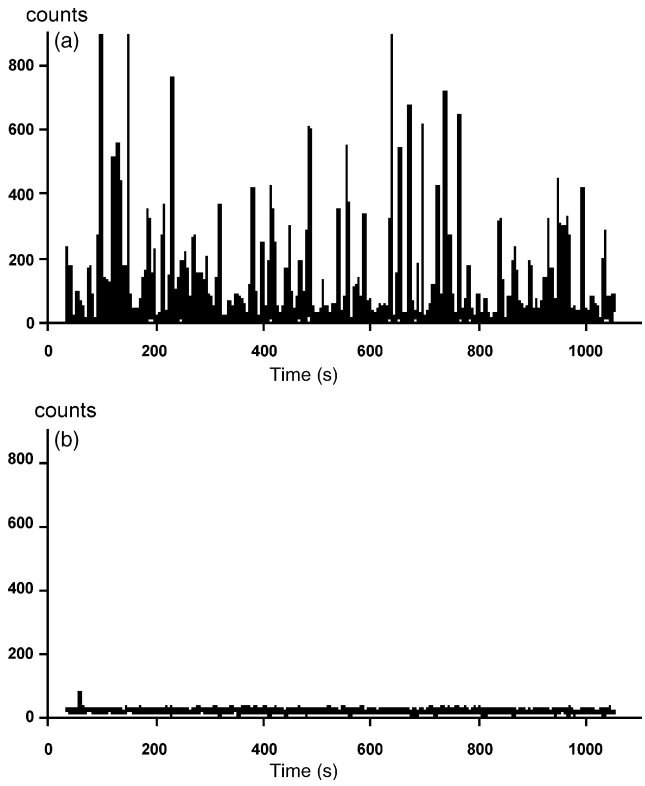

Fig. 2. Variation in the intensity of the $^{132}Xe^+$ mass peak from an irradiated UO_2 fuel with a burn-up of 61 MWd/kgHM as a function of the sputtering time (erosion depth). (a) In a zone where gas bubbles have formed; (b) in a zone where the fission gas was uniformly distributed in the fuel matrix (after Noirot et al. [22]).

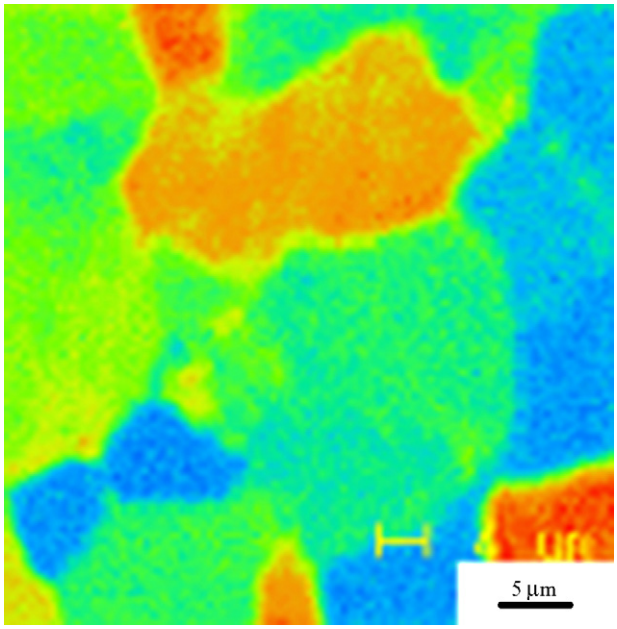

Fig. 3. SIMS ion map ($^{238}U^{16}O^+$) showing the size and morphology of the UO_2 grains at the mid-radius in a PWR fuel. The different grain contrast is due to differences in crystallographic orientation (after Desgranges and Pasquet [23]).

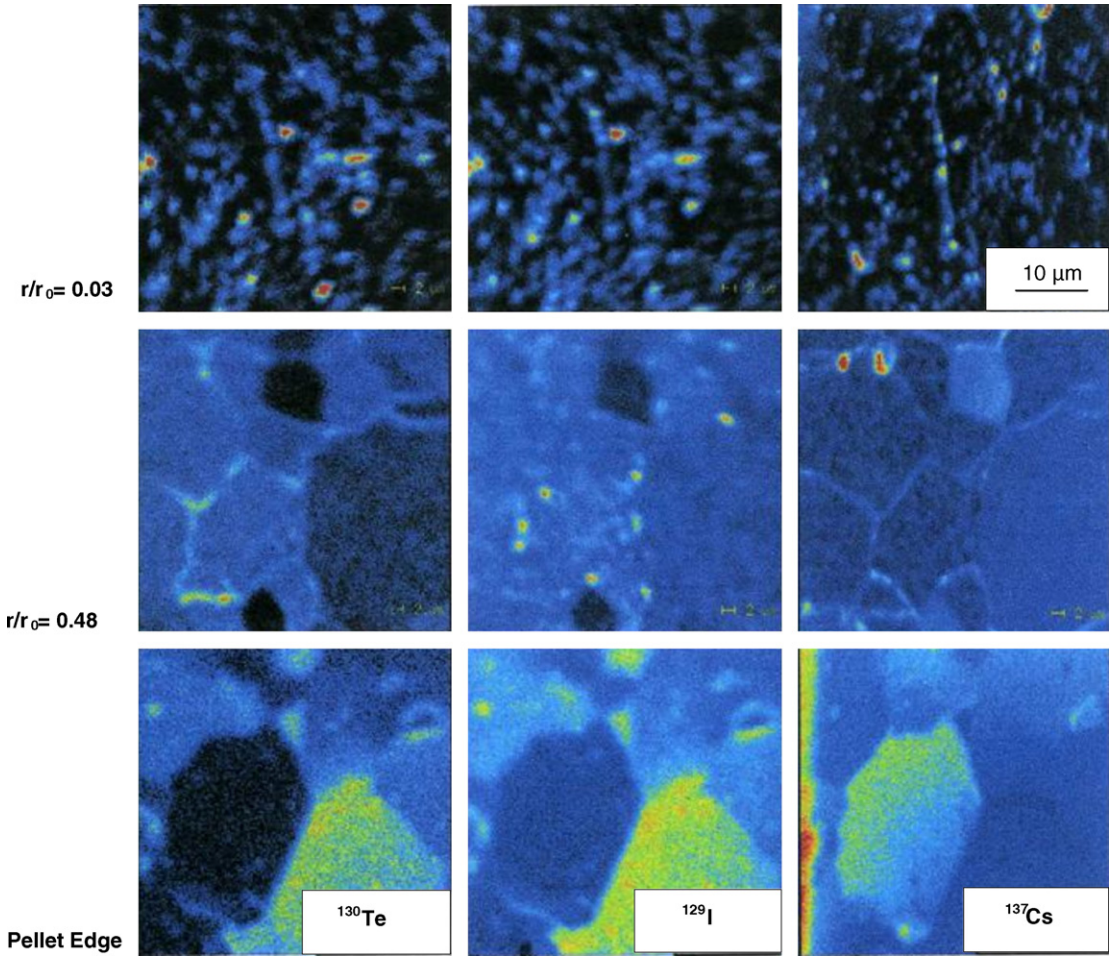

Fig. 4. Ion maps showing the distributions of I, Cs and Te at the pellet edge, mid-radius and pellet centre in a UO_2 fuel ramp-tested to 520 W/cm at a burn-up of 39 MWd/kgHM (after Desgranges et al. [24]).

tion or unless the standard and sample are polycrystals with a similar texture. In the latter case, the analysed area must contain sufficient grains to be representative.

4.2. Behaviour of volatile fission products during a reactor power excursion

Iodine, caesium and tellurium are volatile fission products, which can migrate and leave the fuel during a reactor power ramp. Consequently, to have a better understanding of the fuel behaviour and its evolution during a power ramp, data on the radial distribution of these species after a power ramp are needed. The behaviour of iodine, caesium and tellurium during a power ramp is also one of the main topics in studies of fuel-cladding interaction. Analyses (by SIMS, EPMA and SEM) on UO_2 irradiated samples were performed by Desgranges et al. [24] to understand the behaviour and release mechanisms of these fission products during a power ramp. Samples were prepared from a rodlet that had undergone a ramp test in the OSIRIS reactor. The rodlet was refabricated from an UO_2 rod that had been irradiated in a power reactor to an average burn-up of 35 MWd/kgHM. SIMS ion mapping was performed at five positions along the pellet radius (from the edge to the centre) and the location of the studied species in each of the different fuel zones was identified (see Fig. 4). They found [24] that except at the edge of the sample, iodine forms precipitates during a power ramp, associated with intra- and intergranular fission gas bubbles. They also found that iodine is probably released together with the fission gases because they behave very similarly. This is consistent with the literature [25]. The behaviour of caesium was found to be very different from iodine in that caesium uniformly coats the grain boundaries near the surface of the fuel. Moreover, in this region caesium migration was observed although no gas bubbles had formed. Consequently, Desgranges et al. [24] postulate that in the outer region of the fuel caesium was not present in the gaseous state, but probably as a constituent of a caesium-rich second phase. In this region, the release mechanism is probably solid-state diffusion along the grain boundaries to free surfaces. At higher temperature, nearer to the pellet centre, caesium behaves similarly to the fission gases and is probably released together with them. The behaviour of tellurium appears to be intermediate between that of iodine and caesium, but further investigation is needed to confirm this.

4.3. Mechanism of iodine migration in nuclear fuel

Hocking et al. [26,27] have used SIMS depth profiling to study the migration behaviour of iodine. The work was per-

formed on polished non-irradiated polycrystalline UO_2 (sintered to 97% theoretical density). Samples were annealed under dry conditions (Ar-4%He, 1500 °C) to remove mechanical damage created by polishing before being implanted with various fission products including Rb, Kr, Cs, Xe, Eu, Er and I to simulate irradiated fuel. The implantation energy varied from 300 keV to 1 MeV to obtain near-Gaussian distributions at mean projected ranges of 75 or 150 nm. Implanted-ion doses varied from 1.0×10^{11} to 1.0×10^{16} at/cm^2. The samples were then annealed at temperatures between 1200 and 1650 °C for periods ranging from 10 min to 24 h to cause the ion-implanted fission product layer to broaden by thermal diffusion. Fission fragment damage, which is the second cause of spreading of the iodine distribution, was simulated by 72 MeV iodine-ion bombardment.

Depth profiling on both thermally treated and as-implanted samples were performed using a Cameca IMS-6f. A 10 keV, 30 μm diameter and 30–100 nA Cs^+ primary ion beam was used, scanning an area of 250 × 250 μm. Secondary ions were efficiently extracted from a smaller region (60–100 μm) at the centre of the sputtered area to minimise crater effects. Depth profiles were produced on a thermally treated sample and its as-implanted twin under identical operating conditions in order to obtain information on the spreading of the iodine distribution caused by thermal annealing and ion implantation damage.

The concentration scale for the as-implanted sample was assessed and a relative sensitivity factor (RSF) was then determined for $^{127}I^-$ (normalised to the matrix species) under the conditions used. The application of this RSF to the iodine profiles in the thermally treated samples allowed their concentration scale to be calibrated. Hocking et al. [27] found that at high temperature iodine diffused towards great depths in the tail of the profile as shown in Fig. 5. For iodine concentrations above 1×10^{16} at/cm^3, however, trapping occurs at quasi-immobile defect sites which inhibits diffusive spreading into the bulk matrix [26]. They also report that radiation enhanced diffusion associated with lattice vacancies created during the implantation process caused the implanted iodine ions to migrate towards the sample surface during thermal treatment.

The study reveals the important role of radiation damage on the re-distribution of fission products in the UO_2 fuel. The radiation enhanced diffusion coefficients and the thermal diffusion coefficients obtained in the investigation (at 1400 °C and lower temperatures) were in reasonable agreement with those reported in the literature.

4.4. Radial distribution of Gd in (U,Gd)O_2 fuel rods

The inclusion of (U,Gd)O_2 fuel rods in water reactor fuel assemblies is an integral part of modern reload core management strategy. The Gd isotopes ^{155}Gd and ^{157}Gd have thermal neutron absorption cross-sections of 61,000 and 254,000 barn, respectively, and when added to UO_2 in the form of a few percent of Gd_2O_3 can be used to prolong the fuel cycle and maximise the average fuel burn-up.

During the early stages of irradiation the ^{155}Gd and ^{157}Gd are transmuted to ^{156}Gd and ^{158}Gd with neutron absorption cross-sections of 2.0 and 2.3 barn, respectively. Consequently, when

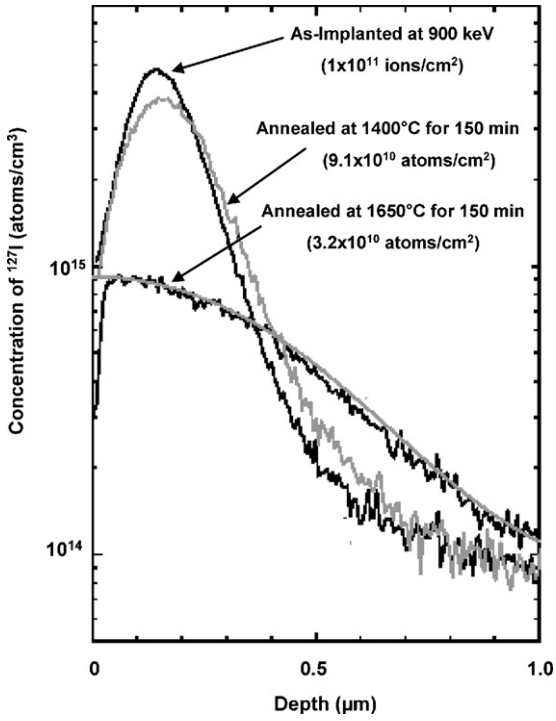

Fig. 5. SIMS depth profiles for $^{127}I^-$ in polycrystalline UO_2, as-implanted and after annealing. During annealing at 1650 °C iodine diffuses to greater depths increasing the concentration in the tail of the profile (after Hocking et al. [27]).

the ^{155}Gd and ^{157}Gd isotopes have been burnt residual neutron poisoning is negligible. Because of the very high absorption cross-sections the burn-out of ^{155}Gd and ^{157}Gd begins at the fuel pellet surface and progresses into the fuel as irradiation proceeds. The self-shielding effect of UO_2 leads to an abrupt interface between the fuel regions containing burnt and unburnt gadolinium which gradually moves towards the fuel centre with time.

Zwicky et al. [28] used SIMS to study the behaviour of Gd_2O_3 "burnable poison" in PWR fuel irradiated to low burn-up (2–6 MWd/kgHM). They measured the radial distribution of the isotopic abundances of ^{154}Gd, ^{155}Gd, ^{156}Gd, ^{157}Gd and ^{158}Gd isotopes in the fuel. In addition to the depletion of ^{155}Gd and ^{157}Gd in the outer region of the fuel between the pellet surface and about $r/r_o = 0.75$ (see Fig. 6) they also detected a slight decrease in their concentration in the central region of the fuel compared with their original natural abundances. They attributed this to resonance reactions with fast neutrons in the flux spectrum.

4.5. Radial distribution of plutonium and radial burn-up profile in MOX fuel

Plutonium from the reprocessing of spent LWR fuel can be recycled by mixing a few percent with UO_2 to produce a mixed oxide (MOX) fuel which is then burnt in a light water reactor. In the frame of the PRIMO Programme, Zwicky et al. [30] used SIMS to determine the radial distribution of plutonium and the radial burn-up profile in MOX fuel pellets that had been irradiated in a PWR to a burn-up between 16 and 55 MWd/kgHM (see Fig. 7).

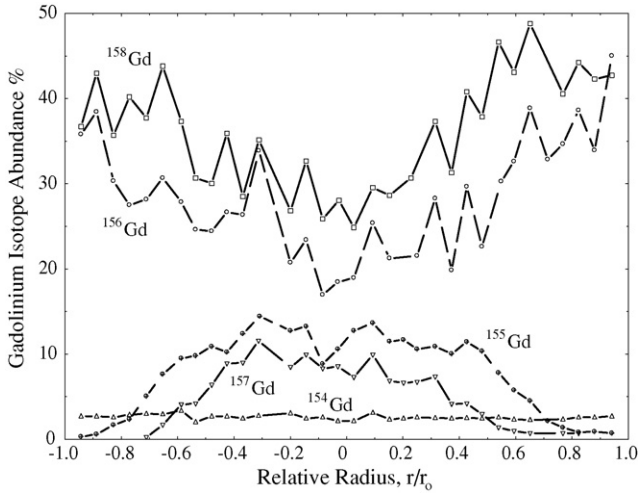

Fig. 6. Distribution of the gadolinium isotopic abundances in a UO_2 fuel doped with up to 7 wt.% Gd_2O_3 as a neutron poison and irradiated to a burn-up of 2 MWd/kgHM (after Bart et al. [29]).

For plutonium, they measured the radial distributions of ^{239}Pu, ^{240}Pu, ^{241}Pu and ^{242}Pu. They concluded that the measured profiles were the result of four nuclear reactions; namely, fission of ^{239}Pu and ^{241}Pu, the formation of ^{239}Pu by neutron capture by ^{238}U, the formation of ^{240}Pu, ^{241}Pu and ^{242}Pu by thermal neutron capture by ^{239}Pu, ^{240}Pu and ^{241}Pu, respectively, and the decay of ^{241}Pu (half-life, 14.4 years).

The radial burn-up profile was assessed from the radial distribution of a number of rare-earth fission product isotopes including ^{148}Nd, ^{140}Ce and ^{139}La. It is evident from the SIMS profiles for these fission products [30], that the radial burn-up distribution in the fuel sample presented in the paper (burn-up, 35 MWd/kgHM) was highly asymmetrical.

4.6. Studies relating to Zircaloy cladding corrosion

Zircaloy cladding corrosion in a PWR depends on the water chemistry [31,32]. Lithium and boron, from the coolant (containing up to 3 μg/g LiOH and 150 μg/g H_3BO_3 in most cases) are incorporated in the Zircaloy external oxide layer during irradiation and have an important influence on cladding corrosion rate [33,34]. Gebhardt and co-workers [6,7,29,35,36] have published the results of several SIMS investigations of the distribution of Li and B in the oxide layer on Zircaloy cladding and Zircaloy control rod guide tubes. These studies were performed on autoclaved and irradiated samples. Ion-implanted samples were used as standards for quantitative analysis. They found that within 1–3 μm of the oxide/metal interface the concentrations of Li and B in the oxide layer on Zircaloy cladding fell sharply to almost zero. The highest concentrations of Li and B were found in the outer (waterside) third of the oxide layer and it was noted that peaks in the B signal generally corresponded to the locations of intensity minima in the Li signal. The Li and B concentrations in the oxide layer on irradiated cladding were reported to range from 8 to 23 and 60 to 190 ppm, respectively.

Autoclave experiments [37] under isothermal conditions revealed that a Li concentration higher than 70 μg/g increases the Zircaloy corrosion rate, but the mechanism is still not well understood. In the oxide layer of irradiated samples cut from the middle and bottom of a PWR fuel rod, it was found [6] that peak concentrations of Li were below the 70 μg/g threshold for both thin (∼10 μm) and thick (∼50 μm) oxide layers. Consequently, for the investigated samples, Li incorporation in the oxide layer could not have bee responsible for enhanced corrosion.

Gebhardt et al. [12] and later Rasser et al. [8] also used SIMS to investigate the behaviour of Fe and Cr (minor alloying elements in Zircaloy) in the oxide layer on Zircaloy cladding. They both report that Cr occurs in the form of precipitates both in the oxide layer and the Zircaloy, whereas Fe is uniformly distributed in the oxide layer, but is present as precipitates in the Zircaloy (see Fig. 8). Recently, similar results have been reported by Brémier et al. [10].

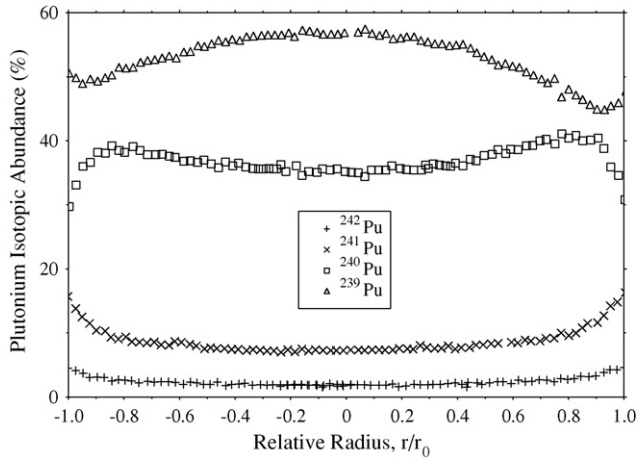

Fig. 7. Radial distribution of plutonium isotopes across the diameter of a MOX fuel (after Bart et al. [29]).

4.7. Isotope ratio measurements

In the frame of safeguards analysis [4,38–41] at the Institute for Transuranium Elements, isotope ratio measurements are being used to determine the $^{235}U^+$ enrichment of UO_2 dust collected at fuel fabrication plants around the globe. The aim is to detect undeclared nuclear activities. As a general rule, a $^{235}U/^{238}U$ ratio greater than about 0.25 (20% enrichment) is taken as an indication of fabrication of weapons grade uranium. Table 5 shows SIMS results for the $^{235}U/^{238}U$ isotopic ratio of three certified UO_2 particles with nominal ^{235}U concentrations

Table 5
SIMS results for the $^{235}U/^{238}U$ isotopic ratio of three uranium particle standards of known enrichment

Nominal ^{235}U conc. (wt.%)	Specified ratio	Measured ratio	Relative difference (%)
2	0.0207	0.0208 ± 0.0004	0.6
10	0.114	0.114 ± 0.002	<0.1
50	1.000	1.009 ± 0.004	0.9

The difference between the measured and specified ratios is less than 1% relative.

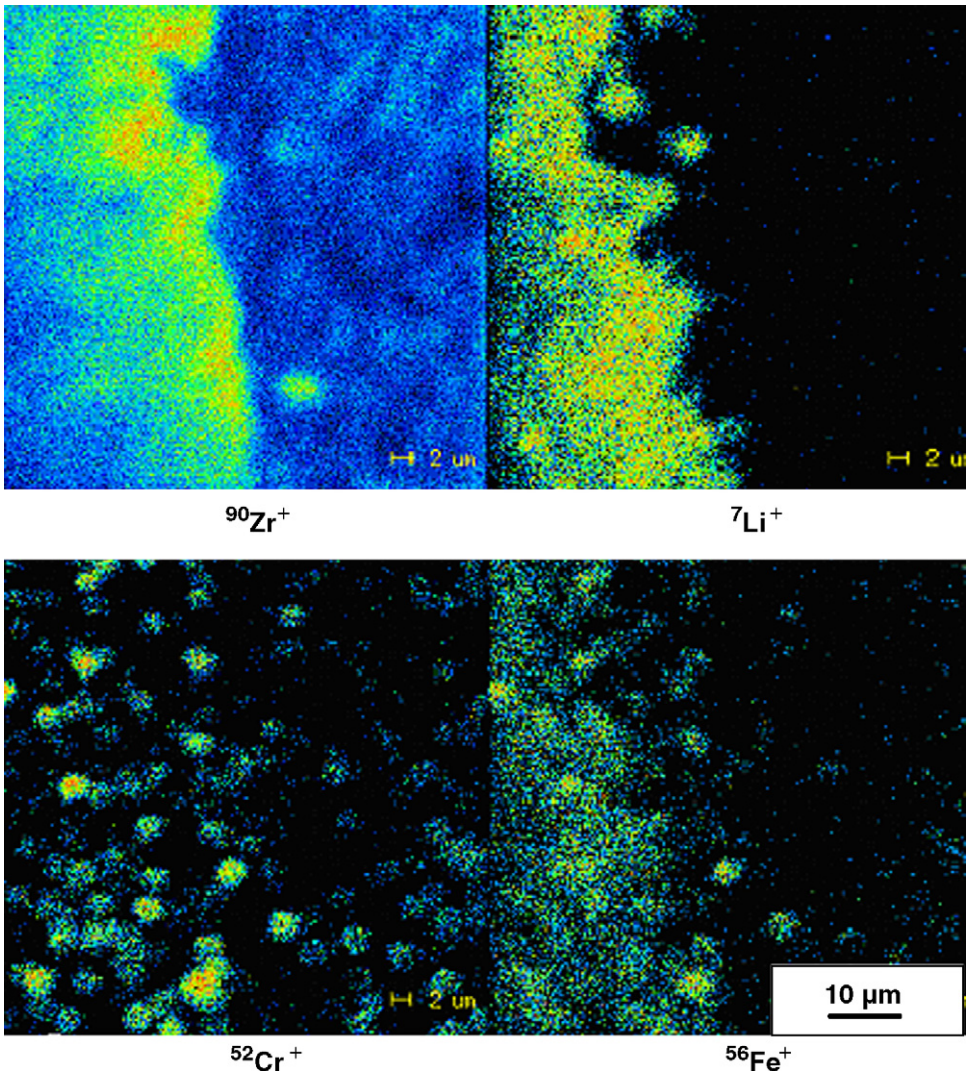

Fig. 8. Ion maps for $^{90}Zr^+$, $^{7}Li^+$, $^{52}Cr^+$ and $^{56}Fe^+$ in the external oxide layer of Zircaloy cladding material (after Rasser et al. [8]). Iron precipitates in Zircaloy partially dissolve in the oxide.

of 2, 10 and 50 wt.% reported by Brémier et al. [10]. The analyses were performed in the microprobe mode using a O_2^+ primary beam at a current of 2 nA. It can be seen that for all three samples the difference between the measured and specified $^{235}U/^{238}U$ ratios is less than 1% relative.

Erdmann et al. [42] have used SIMS to verify the isotopic composition of monodisperse UO_2 particles. In particular, they assessed the contribution of the $^{235}UH^+$ signal to the $^{236}U^+$ signal by using the ratio of the $^{238}U^+$ to $^{238}UH^+$ signals ($^{239}Pu^+$ was absent from the sample). Using this correction, they obtained excellent agreement with certified values of the $^{236}U^+$ isotope concentration and good reproducibility. This work was based on the techniques developed at the Institute for Transuranium Elements by Betti and Tamborini [43–47]. They studied the feasibility of performing SIMS analysis on UO_2 microparticles, containing uranium and plutonium isotopes, and methods of accurately determining the isotopic composition. These studies led to the use of several parent/daughter isotope ratios, e.g., $^{238}Pu/^{234}U$, $^{239}Pu/^{235}U$, $^{240}Pu/^{236}U$ to determine age of reactor produced plutonium [44,47] and the use of the $^{231}Pa/^{235}U$ or $^{234}U/^{230}Th$ isotope ratio to determine the production date of highly enriched uranium [46]. The analytical conditions used for measurement of actinide isotope ratios at the Institute for Transuranium Elements are given in Table 3.

Tamborini et al. [48] has also studied the $^{18}O/^{16}O$ ratio in several UO_2 samples. They demonstrated that this ratio varies as a function of the distance of the production plant from the oceans and with latitude and so could be used as a discriminator in nuclear forensic investigations.

5. Summary and conclusions

The Paul-Scherrer Institute (PSI) at Würenlingen, Switzerland, pioneered the application of SIMS to irradiated nuclear fuel. Bart and colleagues installed the shielded SIMS, which was an ATOMIKA a-DIDA quadrupole mass analyser, there in the late 1970s. Most of the work carried out on this instru-

ment was performed for international fuel and cladding research programmes and under contract to commercial partners and consequently, only a small number of the many SIMS investigations performed are reported in the open literature. Nevertheless, it is apparent from the published articles that the measurements made were restricted mainly to depth profiling and line scanning. Presumably, this was because the low mass resolution and low sensitivity of the quadrupole mass analyser did not permit the production of distribution images of the isotopes of interest, which were usually present in concentrations below 1 wt.%. It is also evident from the literature that over the years the shielded SIMS at PSI was used in a wide range of applications. For example, it was used to measure the radial distributions of Pu isotopes and fission product isotopes in MOX fuel, to study the burnout of gadolinium neutron poison in PWR fuel, to determine the local burn-up in light water reactor fuel, and to investigate Zircaloy cladding corrosion. Gebhardt's innovative results for the distribution of Li and B in the external oxide layer on irradiated Zircaloy cladding demonstrate that isotopes of low mass elements can be located, measured and quantified by SIMS.

With the introduction in 1999 of a shielded CAMECA IMS-6f double-focusing SIMS in the Laboratoire d'Etudes des Combustibles of the CEA Cadarache, France, SIMS became a mature research tool in the study of the in-pile behaviour of nuclear fuel. The device was now no longer restricted to the provision of analytical data on the behaviour of specific isotopes, but began to be used to study the mechanisms controlling such basic phenomena as fission product release and fuel swelling. This change of role can be traced to the fact that with a double-focusing SIMS high resolution, high definition distribution images of isotopes present in trace concentrations can routinely be produced. In the study of the in-pile behaviour of nuclear fuel, SIMS is evidently a powerful complementary technique to EPMA. Its great potential is demonstrated by the fact that in the short period that the SIMS has been in operation at the CEA Cadarache, it has supplied important data on the behaviour of the volatile fission products Te, I and Cs during a reactor power ramp. For example, it has confirmed that I behaves similar to the fission gas Xe during a reactor power excursion.

In 2003, the Institute for Transuranium Elements also acquired a shielded CAMECA IMS-6f double-focusing SIMS. It is foreseen that this instrument will be used to determine the distribution of fission product and actinide isotopes in UO_2 high burn-up fuel and in the Pu-spots and matrix of MOX fuel irradiated under steady-state and transient conditions. In addition, it will be used to investigate the transmutation efficiency in fuel targets containing the minor actinides Np, Am and Cm and to determine the fission product and actinide concentration profiles at the surface of spent nuclear fuel after leaching. The main challenge in the near future is to develop quantification procedures that can be used to convert the measured ion signal to mass concentration. This will require the preparation of bulk and ion-implanted standards imitating the chemical composition of the material to be analysed, the compilation of a database of relative sensitivity factors, and where appropriate correlation with element analysis carried out by EPMA on the same area of the sample.

References

[1] C.T. Walker, J. Anal. At. Spectrom. 14 (1999) 447.
[2] C.T. Walker, J. Nucl. Mater. 80 (1979) 190.
[3] C.T. Walker, J. Trace Microprobe Tech. 15 (1997) 419.
[4] M. Betti, Int. J. Mass Spectrom. 242 (2005) 169.
[5] G. Bart, T. Aerne, U. Flückiger, E. Sprunger, Nucl. Instrum. Methods 180 (1981) 109.
[6] O. Gebhardt, Fresnius J. Anal. Chem. 365 (1999) 117.
[7] O. Gebhardt, D. Gavillet, L. Ottvi, J.Y. Blanc, J. Thomazet, Proceedings of the IAEA Technical Committee Meeting on Water Chemistry and Corrosion Control on Cladding and Primary Circuits Components, Libcice-Vitavou, Czech Republic, 28 September–2 October 1998, Report IAEA-TECDOC-1128, 1999, p. 151.
[8] B. Rasser, L. Desgranges, B. Pasquet, Appl. Surf. Sci. 203 (2003) 673.
[9] L. Desgranges, B. Pasquet, B. Rasser, Proceedings of the IAEA Technical Meeting on Advanced PIE Techniques for Water Reactor Fuels, Dimitrovgrad, Russia, May 2001, IAEA-TECDOC-1277, 2002, p. 105.
[10] S. Brémier, R. Hasnaoui, S. Portier, O. Bildstein, C.T. Walker, Proceedings of the Meeting IUMAS-3 and 9th EMAS European Workshop on Modern Developments and Applications in Microbeam Analysis, Microchim. Acta 155 (2006) 113.
[11] W.H. Hocking, R.A. Verrall, P.G. Lucuta, Hj. Matzke, Radiat. Eff. Defects Solids 125 (1993) 299.
[12] O. Gebhardt, T. Aerne, M. Martin, S. Tao, N. Loibl, K. Wittmaack, in: H.J. Mathieu, B. Reihl, D. Briggs (Eds.), Proceedings of ECASIA'95, John Wiley & Sons Ltd., Chichester, UK, 1996, p. 389.
[13] R.A. Burdo, G.H. Morrison, Table of Atomic and Molecular Lines for Spark Source Mass Spectrometry of Complex Sample–Graphite Mixes, Department of Chemistry, Cornell University, Ithaca, NY, USA, internal report 1670.
[14] R. Manzel, C.T. Walker, J. Nucl. Mater. 301 (2002) 170.
[15] R.G. Wilson, F.A. Stevie, C.W. Magee, Secondary Ions Mass Spectrometry: A Practical Handbook for Depth Profiling, Wiley, New York, 1989, p. 3.1-1.
[16] D.P. Leta, G.H. Morrison, Anal. Chem. 52 (1980) 514.
[17] PC1 User's Manual for CAMECA SIMS Instruments, C. Evans and Assoc., Redwood City, California, USA, 1987.
[18] D. Phinney, Microsc. Microanal. 12 (2006) 352.
[19] M.A. Ray, J.E. Baker, C.M. Loxton, J.E. Greene, J. Vac. Sci. Technol. A6 (1988) 44.
[20] L. Desgranges, B. Pasquet, Nucl. Instrum. Methods, Sect. B 215 (2004) 545.
[21] J. Lamontagne, J. Noirot, L. Desgranges, T. Blay, B. Pasquet, I. Roure, Microchim. Acta, Part B 145 (2004) 91.
[22] J. Noirot, L. Noirot, L. Desgranges, J. Lamontagne, T. Blay, B. Pasquet, E. Muller, Proceedings of the ANS International Topic Meeting on LWR Fuel Performance, ANS La Grange Park, IL, 2004, paper 1019.
[23] L. Desgranges, B. Pasquet, Proceedings of the 21st Plenary Meeting of European Working Group on Hot Laboratorie and Remote Handling, Saclay, France, September 22–24, 2003, p. 21.
[24] L. Desgranges, B. Pasquet, X. Pujol, I. Roure, Th. Blay, J. Lamontagne, Th. Martella, B. Lacroix, O. Comiti, L. Caillot, Proceedings of the NEA/NSC International Seminar on Pellet/Clad Interactions with Water Reactor Fuels, Aix-en-Provence, France, 2004, p. 241.
[25] M. Peehs, G. Kaspar, K.H. Neeb, J. Nucl. Mater. 119 (1983) 284.
[26] W.H. Hocking, R.A. Verrall, S.J. Bushby, Proceedings of the IAEA Technical Committee Meeting on Fuel Cycle Options for Light Water Reactors and Heavy Water Reactors, IAEA-TECDOC-1122, 1999, p. 111.
[27] W.H. Hocking, R.A. Verrall, I.J. Muir, J. Nucl. Mater. 294 (2001) 45.
[28] H.U. Zwicky, T. Aerne, G. Bart, F. Petrik, H.A. Thomi, Radiochim. Acta 47 (1989) 9.
[29] G. Bart, O. Gebhardt, E.T. Aerne, M. Martin, Proceedings of the IAEA Technical Committee Meeting on Development of Post-irradiation Examination at the Reactor Fuel Examination Facility, IAEA-TECDOC-822, 1995, p. 337.

[30] H.U. Zwicky, T. Aerne, A. Hermann, H.A. Thomi, M. Lippens, J. Nucl. Mater. 202 (1993) 65.
[31] C. Lemaignan, A.T. Motta, in: R.W. Cahn, P. Haasen, E.J. Kramer (Eds.), Materials Science and Technology. Part II: Nuclear Materials, vol. 10B, VCH Verlagsgesellschaft GmbH, Weinheim, Germany, 1994, p. 1.
[32] P. Billot, B. Cox, K. Ishigure, A.B. Johnson, C. Lemaignan, A.F. Nechaev, N.G. Petrik, E.A. Reznichenko, I.G. Ritchi, G.I. Sukhanov, Proceedings of the IAEA Technical Committee Meeting on Corrosion of Zirconium Alloys in Nuclear Power Plants, IAEA-TECDOC-684, 1993.
[33] O. Gebhardt, A. Hermann, Electrochim. Acta 41 (1996) 1181.
[34] L.O. Actis-Dato, PhD Thesis, Etude par Spectrométrie de Masse à Décharge Luminescente de la Diffusion d'Impuretés Chimiques dans des Couches d'Oxyde de Zirconium, IPN University of Orsay, France, 2000.
[35] O. Gebhardt, D. Gavillet, J. Nucl. Mater. 279 (2000) 368.
[36] O. Gebhardt, E.T. Aerne, Y. Gao, D. Renard, K. Wittmaack, Proceedings of the German SIMS Forum, Berlin, October 4–5, 1995.
[37] H.G. Weidinger, H. Ruhmann, G. Cheliotois, M. Maguire, T.L. Lau, ASTM-STP 1132, 1992, p. 499.
[38] S. Letho, Development of a SIMS Method for Isotopic Analysis of Uranium Containing Particles, Report on task FIN A 1318 of the Finnish Support Programme to IAEA safeguards, STUK-YTO-Tr 188, 2002.
[39] D.L. Donahue, Anal. Chem. 1 (2002) 28A.
[40] F.G. Rüdenauer, Y. Kuno, P.M. Hedberg, S. Vogt, M. Kohl, F. Pilchmayer, Proceedings of the 42nd INMM Annual Meeting, Indian Wells, California, USA, 2001 (abstract no. 159).
[41] S. Sakurai, et al., Proceedings of the 42nd INMM Annual Meeting, Indian Wells, California, USA, 2001 (abstract no. 249).
[42] N. Erdmann, M. Betti, O. Stetzer, G. Tamborini, J.V. Kratz, N. Trautmann, J. van Geel, Spectrochim. Acta B 55 (2000) 1565.
[43] G. Tamborini, PhD Thesis, Développement de la Technique SIMS pour l'Analyse de Particules Radioactives et ses Applications à Différents Echantillons, University of Paris-Sud, Orsay, France, 1998.
[44] G. Tamborini, M. Wallenius, O. Bildstein, L. Pajo, M. Betti, Mikrochim. Acta 139 (2002) 185.
[45] G. Tamborini, M. Betti, V. Forcina, T. Hiernaut, B. Giovannone, L. Koch, Spectrochim. Acta B 53 (1998) 1289.
[46] G. Tamborini, M. Betti, Mikrochim. Acta 132 (2000) 411.
[47] M. Betti, G. Tamborini, L. Koch, Anal. Chem. 71 (1999) 2616.
[48] G. Tamborini, D. Phinney, O. Bildstein, M. Betti, Anal. Chem. 74 (2002) 6098.
[49] N.S. McIntyre, C.G. Weisener, R.D. Davidson, A. Brennenstuhl, B. Warr, J. Nucl. Mater. 178 (1991) 80.
[50] M. Asuvathraman, S. Rajagopalan, K. Ananthasivan, C.K. Mathews, R.M. Mallya, J. Nucl. Mater. 224 (1995) 25.
[51] O. Gebhardt, M. Gehringer, Th. Graber, A. Hermann, Mater. Sci. Forum 192–194 (1995) 587.